Relationship between Nano and Macroscale Properties of Post-fire ASTM A36 Steels

Dharanidharan Arumugam[1], Dayakar L. Naik[2] , Hizb Ullah Sajid[3], and Ravi Kiran[4]

Abstract

In this study, we investigated the composition and mechanical properties of metallurgical phases present in the ASTM A36 steels subjected to post-fire temperatures using nanoindentation testing in conjunction with K++ clustering method. The specimens are exposed to target temperatures from 500°C to 1000°C with an increment of 100°C. We extracted 500°C, 600°C, 700°C, 800°C, 900 °C, and 1000°C and two important nanomechanical properties, namely hardness, and Young's modulus from the nanoindentation tests and used it as descriptive features for the clustering analysis. Results obtained from this analysis show that average volume fraction percentage of ferrite and pearlite was 84% and 16%, respectively. The results also revealed that the mean hardness values were in the range of 2.46 to 3.01 GPa for ferrite and 3.11 to 4.27 GPa for pearlitefor the different temperature exposures. The Young's modului of ferrite ranged from 171.7 to 203.3 GPa, whereas the pearlite phase ranged from 181.1 to 206.8 GPa for the different temperature exposures. The obtained results also indicated the existence of a quadratic correlation between the pearlite's mean nanoindentation hardness and the yield and tensile strength of different post-fire ASTM A36 steels. **Keywords:** Clustering; Ferrite; Pearlite; Nanoindentation; Phase composition; and Nanohardness.

[1] Graduate Research Assistant, Dept. of Civil & Environmental Engineering, North Dakota State University, Fargo, ND 58105, email: d.arumugam@ndsu.edu

[2] Research Associate, Dept. of Civil & Environmental Engineering, North Dakota State University, Fargo, ND 58105, email: dayakarnaik.lavadiya@ndsu.edu

[3] PhD Candidate, Dept. of Civil & Environmental Engineering, North Dakota State University, Fargo, ND 58105, email: hizbullah.sajid@ndsu.edu

[4] Assistant Professor (corresponding author), Dept. of Civil & Environmental Engineering, North Dakota State University, Fargo, ND 58105, email: ravi.kiran@ndsu.edu

1. Introduction

The crucial part of any alloy development or material design is to systematically understand the properties of microstructural constituents so that they can be engineered to attain desired properties at the macroscale. The macroscale material properties are used for the design of structural components. In the case of structural steels, the mechanical properties such as strength and ductility can be tailored by changing the composition and sizes of microstructural constituents referred to as metallurgical phases, namely ferrite, pearlite, bainite, martensite, cementite, and austenite (Campbell 1967; Elwazri et al. 2005; Igwemezie et al. 2016; Jiang et al. 1995; Kumar et al. 2008; Sajid et al. 2020). Alternatively, the composition and size (grain size) of these microstructural constituents also provide valuable insights into the thermal loading and heat treatment history that structural steels undergo during production and service life. Hence, understanding and evaluating these microstructural properties can play a crucial role in post-fire investigations and evaluation of the post-fire mechanical properties of structural steels (Sajid et al. 2020). Moreover, understanding the post-fire mechanical properties is integral to determining the post-fire usability of steel structures and hence determining the post-fire mechanical properties of a wide range of structural steels (mild steels (Ding et al. 2019; Lu et al. 2016; Outinen and Mäkeläinen 2004; Sajid and Kiran 2018; Sajid et al. 2020; Smith et al. 1981; Zhang et al. 2020), high strength steels (Aziz and Kodur 2016; Chen et al. 2016; Chiew et al. 2014; Kang et al. 2018; Lee et al. 2012; Li et al. 2017; Qiang et al. 2012; Sajid and Kiran 2019; Sajid et al. 2020; Siwei et al. 2017; Smith et al. 1981; Wang and Lui 2020; Wang et al. 2015; Zhang et al. 2020; Zhu et al. 2021), very high strength steels (Azhari et al. 2015; Qiang et al. 2013), cold-formed and cast steels (Gunalan and Mahendran 2014; Lu et al. 2017; Ren et al. 2020; Yan et al. 2021), and stainless steels (Ban et al. 2020; Tao et al. 2018)) has been the subject of the many studies that were conducted in the past decade. An extensive review of the existing literature on the post-fire mechanical behavior of structural steels suggests that post-fire mechanical properties of structural steels can be quantified using three different approaches, namely 1) post-fire residual factors, 2) color-based visual examination, and 3) microstructure-based approach. Post-fire residual factor equations have been proposed in the literature for different structural steels. These residual factor equations can be used to accurately estimate the post-fire mechanical properties of structural steels exposed to a particular temperature that was reached during a fire accident. The existing post-fire residual factors employ the fire temperature as the main variable, and hence they rely on accurate knowledge of temperatures reached during fire accidents. The visual examination approach facilitates the determination of fire temperatures based on the surface oxide colors of post-fire structural steels (Colwell and Babic 2012). Surface oxides exhibit different colors at different temperatures, and hence these colors can be used as an approximate indication of temperatures reached during a fire accident. The temperatures obtained from the visual examination can be used in conjunction with the post-fire residual factor equations to estimate the post-fire mechanical properties of structural steels. The visual examination approach is subjective, and the temperatures obtained may change with the steel exposure time and conditions at room temperature. The microstructural approach overcomes the limitations of the first two approaches, and it can be used to determine the post-fire mechanical properties using the composition and sizes of the metallurgical phases that are present in the structural steels after fire accidents (Sajid et al. 2020). The microstructure-based approach can be used to accurately predict the post-fire mechanical properties of structural steels without the knowledge of temperatures that were reached during fire accidents.

The microstructure-based approach for post-fire mechanical properties estimation relies on accurate evaluation of composition and sizes of metallurgical phases that are present in the structural steels. The metallurgical phases in structural steels are often identified through optical methods or electron backscatter diffraction techniques in conjunction with well-established iron-iron carbide ($Fe–Fe_3C$) constitutional diagrams, and these methods are proven to yield reliable results (Kamaya 2009; Krauss 2015; Leng 2009; Sajid et al. 2020; Schwartz et al. 2009). The grain sizes corresponding to each metallurgical phase can be obtained using ASTM E112 (2013) specifications. The accuracy of these techniques relies on the proper preparation of specimens and lighting conditions of the micrographs. Apart from these techniques, the characterization of microstructures using nanoindentation tests has shown promising results in the quantitative evaluation of materials such as metals, films, etc. (Bahr et al. 1998; Gain and Zhang 2020; Menčík et al. 1997; Oliver and Pharr 1992; Schuh 2006; Tsui et al. 1996; Tuninetti et al. 2021). Currently, the nanoindentation properties of metallurgical phases in materials can only be determined with the prior knowledge of existing metallurgical phases in the material. In addition to that, the location of the indentations needs to be mapped with microstructural imaging to ascertain the properties of individual metallurgical phases. Alternatively, the material section to be characterized is homogenized with a single metallurgical phase to identify the nano or micro properties (Li et al. 2020). These techniques are both labor-intensive and time-consuming and, in some cases, not viable. Interestingly, with the help of machine learning techniques and by utilizing the nanoindentation values alone, it is possible to characterize the nano-level properties of the microstructures present in the materials. In the case of structural steels, nanoindentation tests can facilitate the evaluation of the nanoscale properties of metallurgical phases, including hardness and Young's modulus. Moreover, nanoindentation test data can also be used to estimate the composition of metallurgical phases that are present in the structural steels, which can subsequently facilitate the determination of post-fire mechanical properties.

This study aims to quantify the metallurgical compositions and nanomechanical properties of phases present in post-fire ASTM A36 steels as a function of fire exposure temperatures using nanoindentation and clustering techniques. Furthermore, the relationship between the nano and macroscale properties are investigated for post-fire ASTM A36 steels. This manuscript is organized as follows: the nanoindentation procedure employed is explained in Section 2, details pertaining to the dataset is described in Section 3, a brief explanation of the clustering technique is provided in Section 4, the validation and impacts of results are discussed in Section 5, and the important conclusions arrived in the study is provided in Section 6.

2. Experimental procedure

In this study, the nanoindentation properties of ASTM A36 steel specimens after exposure to six different high temperatures (500°C, 600°C, 700°C, 800°C, 900 °C, and 1000°C) are evaluated. In addition, the nanoindentation tests are also conducted for the as-received steel specimens. The nanoindentation tests for as-received and post-fire steel specimens are conducted at room temperature. The chosen target temperatures are normally experienced by the structural steels during fire accidents (Sajid and Kiran 2018), and thus the determination of the microstructural properties of these post-fire steel specimens would provide valuable information about the post-fire performance of the ASTM A36 and similar grade steels. The target exposure temperatures employed in this study are also deemed to capture the variation of phase compositions and their properties in ASTM A36 steel as a function of temperature (Sajid et al. 2020). All the test specimens, except the one extracted from the as-received steel, are first heated to the target temperature in an electric furnace with a constant heating rate of 10 °C/min (± 2 °C/min) with a soaking time of 2 hours at the target temperature followed by cooling to the room temperature by placing them outside the oven. An initial temperature of 100 °C was selected before ramping up the temperature to a selected target temperature. The specimens were left to cool naturally in open air at room temperature (27 °C) and it took about 1 hour for specimens to revert to room temperature. More details regarding the preparation of specimen can be found here(Sajid and Kiran 2018; Sajid and Kiran 2019; Sajid et al. 2020). Microstructural images of test specimens are then acquired using Amscope® optical microscope at 50X magnification to study the microstructure of these air-cooled specimens. The microstructural images showed that all the air-cooled steel specimens and the as-received steel specimen had ferrite-pearlite microstructure and agreed with the previous study conducted by the authors (Naik et al. 2019). For illustration purposes, the microstructural images of the as-received steel specimen and the specimen air-cooled from 500°C are presented in Fig. 1. After the microstructural examination, nano-indentation testing is performed on all the specimens.

Nanoindentation has now become a preferred technique to evaluate the mechanical properties of bulk materials and thin films at the micron or sub-micron scale (De Bono et al. 2017; Nguyen et al. 2018; Oliver and Pharr 1992; Pham and Kim 2017; Schwarm et al. 2017; Tatar 2021; Tatar et al. 2019; Zhu and Xuan 2010). In nanoindentation, an indenter is used to penetrate the surface of the materials or films. The relationship between the load applied by the indentor and the resulting indentation depth allows us to determine the elastic and plastic properties of the material. Indenters can be of different geometries such as spherical, conical, cubical, and pyramidal, and they can also be made up of different materials such as diamond, titanium, tungsten, silicon, and/ or steel (Mann 2005). Berkovich (three-sided pyramid shape with a face angle of 65.3° with respect to the vertical indentation axis), Vickers (four-sided pyramid with a face angle of 68°), Knoop (four-sided pyramid with asymmetrical faces), and cube corner (three-sided pyramid with a face angle of 35.3°) are some of the commonly used nanoindenters (Sagadevan and Murugasen 2014). Among the various nanoindenters, Berkovich indentors are widely used for their constant area to depth ratio (which makes the measured hardness independent of load), sharpness (which leads to measurement of smaller testing volume), and ease of manufacturability (Liu et al. 2014). The nanoindentations in the current study are performed using Hysitron TI980 triboindenter nanomechanical system, which employs a standard three-sided pyramid Berkovich nanoindenter with diamond probe tip for the nanoindentation. The indentations are made over a grid that consisted of 15×15 indentation points, totaling 225 indentations, with a spacing of 35 μm, as shown in Fig. 2. To obtain the volume fraction from the surface distribution of the phases and to identify the individual phase properties, the grid design is formulated based on the Gedanken experiment (Pham and Nguyen 2021). As per the Gedanken experiment, nanoindentation depth should be lesser than 1/10th of the characteristic size of the microstructure and also, the spacing of the indentations (l) should be greater than $D/\sqrt{N}$ to avoid any interference from neighboring indentation points and act as an unbiased statistical measure, where D refers to the characteristic size of the microstructure and N refers to the total number of indentation points. ASTM A36 steel specimens used in our current experiment contain only two metallurgical phases, namely ferrite and pearlite and their average sizes are in the range of 9-13 μm and 3-4 μm, respectively. The nanoindentation depths observed in our experiments are well within the range of 250 nm which is less than 1/10th of the characteristic size of the microstructure and 35 μm the spacing adopted is way greater than $D/\sqrt{N}$ which is 0.9μm ($13\mu m/\sqrt{225}$). The nanoindentation test is performed by employing the standard quasi-static approach wherein the load is applied and removed with a constant displacement rate. A load-penetration depth (displacement) curve is generated at the end of the nanoindentation process by plotting incremental penetration depths against the indenter load applied measured using a transducer. The load-penetration depth curve obtained for both the phases of the as-received ASTM A36 steel specimen is presented in Fig. 3b. A typical load-penetration depth curve of a nanoindentation test is also shown in Fig. 3a for the purpose of illustration, and it is clear from Fig. 3b that the obtained nanoindentation curve is qualitatively similar to the ones obtained for other metallic materials (Gadelrab et al. 2012; Mazaheri et al. 2015; Schwarm et al. 2017). As shown in Fig. 3b the nanoindentation is performed till a maximum displacement of 250 nm is reached. After that, the material is unloaded till the load reaches zero and the depth corresponding to the zero-load stage is called the final indentation depth h_f. The unloading part of the curve was fitted with a power relation provided in Eq.1 to obtain the stiffness value, $S = dP/dh$ – which is the slope of the initial tangent drawn at the start of the unloading curve.

$$P = \alpha\,(h - h_f)^m \tag{1}$$

where, α, m are fitting parameters, h_f is the final indentation depth, P and h are instantaneous load and indentation depth, respectively. Finally, the two material properties of interest, hardness and Young's modulus of the steel phases in the nanoindented domain, are determined from these parameters using Oliver-Pharr's method (Oliver and Pharr 1992; Tsui et al. 1996).

Hardness values for the ferrite and pearlite phases present in ASTM A36 steel are determined based on the maximum load and the projected contact area and is computed from the following expression

$$H = P_{max} / A_c \tag{2}$$

where, A_c is the projected contact area of the indenter at the peak load (P_{max}) and it is a function of contact depth, h_c. Both these parameters were calculated using Oliver-Pharr's method. The expression to calculate the contact depth, h_c is written as follows.

$$h_c = h_{max} - \gamma P_{max}/S \tag{3}$$

Here, h_{max} is the maximum indentation depth and S is stiffness or slope of the unloading curve (refer Fig. 3a). The parameter, $\gamma = 0.75$ for sharp indenters.

The reduced Young's modulus is calculated from the projected contact area, A_c and stiffness value, S, of the unloading curve using the following expression:

$$E_r = {\sqrt{\pi}} \Big/ {2\sqrt{A_c}} \; S \tag{4}$$

This reduced Young's modulus is a composite modulus representing the stiffness of both the material and indenter, and it is related to the Young's modulus of the material as follows

$$\frac{1}{E_r} = \frac{1-\nu^2}{E} + \frac{1-\nu_i^2}{E_i} \tag{5}$$

where, E and ν are Young's modulus and Poisson's ratio of the material, respectively, and E_i and ν_i are Young's modulus and Poisson's ratio of the indenter. For Berkovich diamond indenter tip, E_i is *1140 GPa* and ν_i is 0.07. Poisson's ratio of the ASTM A36 steel used in this study is 0.3 (Shen 2019). The Young's modulus values of the phases of the ASTM A36 steel were then calculated from the reduced Young's modulus by substituting the above-stated values in Eq. 5.

The distribution of the hardness and Young's modulus values obtained in the nanoindentation tests for ASTM steels air-cooled from various elevated temperatures, including the as-received steel, are plotted in the form of contours and the contours for target temperatures of 27°C, 500°C, and 900°C are presented in Fig. 4. The higher valued regions in nanoindentation hardness contours are conceivably the regions of pearlite colonies because pearlite, a laminar mixture of ferrite and iron carbides, usually have higher hardness than ferrite due to the presence of iron carbides (Debehets et al. 2014).

3. ASTM A36 Nanoindentation Dataset

A master dataset was constructed from the data obtained from the nanoindentation experiments (described in section 2). The dataset was denoted by $\mathcal{D} \in \mathbb{R}^{p \times q}$, where p indicates the total number of observations and q indicates the number of descriptive features. Every row of the dataset $\mathcal{D}$ is referred to as an instance vector, $\boldsymbol{x}_j = (x_{j1,} \cdots, x_{jq})$, where $x_{j1,} \cdots, x_{jq}$ were the descriptive feature values. Here, j ranges from $1\ to\ p$. In our case, the total (p) number of observations obtained from the experiments was 1575 with a subset of 225 observations corresponding to each ASTM A36 metallographic specimen air-cooled from one of the six different elevated temperatures and one at room temperature. The two descriptive features are the two nanoindentation properties, namely

Young's modulus and hardness determined from the nanoindentation testing at a grid point. It is important to highlight that the generated dataset was 'unlabeled' as it did not contain any response/target variables.

4. Research Methodology

Clustering analysis is a type of unsupervised machine learning technique that deals with unlabeled datasets with no target features (1978; Everitt et al. 2001; MacQueen 1967; Rui and Wunsch 2005). It is a data mining tool used to learn structures or embedded patterns present in a dataset. Clustering algorithms divide and group the instances or data points in a given dataset into a number of subsets in such a way that the similarity (based on certain measures) between the instances that belong to the same subset is high, and the similarity between the instances of different subsets is low. Centroid-based clustering (Bezdek et al. 1984; Li and Wu 2012; Lloyd 1982; Ostrovsky et al. 2006) construct groups based on the proximity of instances to the cluster centroids, density-based clustering (Ester et al. 1996; Kriegel et al. 2011; Sander et al. 1998) employing density threshold to delineate the groups and, hierarchical clustering (Defays 1977; Griffiths et al. 1984; Sibson 1973), which recursively partition the data into tree clusters based on the hierarchical order are some of the popular approaches used for clustering of data.

'K-means' is one of the widely used centroid-based clustering techniques. It was first proposed, though with a different name, by Forgy in 1965 (Lloyd 1982; MacQueen 1967). Among many partition techniques, K-means is preferred for its faster convergence and easy implementation (Li and Wu 2012; Ostrovsky et al. 2006). K-means is also suitable when knowledge about the number of clusters in which a dataset will be partitioned is available, and the dataset is less noisy or having only a few outliers. K-means is an iterative algorithm that partitions a given data set, $\mathcal{D} \in \mathbb{R}^{p \times q}$ with p instances (experimental observations) and q descriptive features, into K predefined clusters, $(\mathcal{D}_1, \mathcal{D}_2, \ldots, \mathcal{D}_k)$. Initially, hardness and Young's modulus of the microstructure obtained from the nanoindentations were tried as the descriptors. However, the preliminary analysis indicated the lack of discriminatory power of Young's modulus in constructing the clusters, thus excluded from the analysis, and only the nanoindentation hardness of the microstructure was used as a descriptive features. This is due to the fact that Young's modulus of ferrite does not significantly differ with the pearlite Young's modulus (Freitas et al. 2009; Hutasoit et al. 2013; Li et al. 2019; Watanabe et al. 2011). This is also clearly seen in Fig. 9a where the mean values of Young's modulus of ferrite and pearlite phases obtained in the clustering analysis are nearly same at all the post-fire temperatures. The partitioned clusters do not share any instances between them. The algorithm starts with a random selection of K number of instances in the dataspace to represent the centroids of the K predefined clusters. For our case, K was taken as 2 as the instances can only belong to one of two metallurgical phases present in the steel specimens.

K-means, in its original form, is sensitive to the initial centroids and may form poor clusters if the randomly selected centroids are not far from each other. To overcome this problem, an alternative seeding technique augmented with K-means algorithm, called K-means++ was proposed in the literature (Arthur and Vassilvitskii 2006). The current study utilized this approach for seeding, and the initial centroids are selected in such a way that they are far away from each other. After initializing the centroids, the instances closer to those centroids are identified and associated with those centers which then are formed into individual clusters. The closeness of the instances from the seeded centroid is evaluated based on the choice of centroidal measure. Euclidean distance is generally used when the centroid is based on the arithmetic mean of instances in a cluster, and Manhattan distance is usually employed as a proximity measure when the median of the points in a cluster is chosen as a centroid. In the current study, we used Euclidean distance to measure the closeness of the instances. Based on the newly formed clusters, a new set of centroids are calculated, and the process is repeated. This recursion is continued until the intra-class variance between the clusters is minimized and the optimal clusters are identified. The flowchart of the research methodology adopted in this study is provided in Fig. 5.

5. Results and Discussion

5.1. Mean hardness and Young's modulus of ferrite and pearlite phases

The volume fractions of the clusters resulted from the K++ means clustering (described in section 4) are depicted in Fig. 6 for the different heat-treated ASTM A36 steel specimens, and the values ranged from 79% to 89% for cluster A and 11% to 21% for cluster B. In an earlier study conducted by the authors (Naik et al. 2019), the metallurgical phases present in these post-fire ASTM A36 steel sections and their composition were identified using a novel texture recognition machine learning classification approach. The published study reported phase compositions for ASTM A36 steel sections air-cooled from the elevated temperatures employed in the current study. This comparison between the results published by Sajid. et al., 2020 (Sajid et al. 2020), and the current investigation is presented in Fig. 7. The comparison clearly indicates that cluster A corresponds to the ferrite phase and cluster B corresponds to the pearlite phase. Hence, the proportion of instances corresponding to each cluster A and cluster B represents the phase compositions of ferrite and pearlite present in the ASTM A36 steel. With this proposed approach, we estimated the average volume fractions of ferrite and pearlite as 84% and 16%, respectively. Another significance of the results is that nanoindentation properties such as hardness and Young's modulus of ferrite and pearlite phases and their variation over the different heat exposures can now be understood. It is clear from Fig. 6 that increase in the temperature exposure of the steel does not affect the phase composition of the steel significantly.The mean hardness values of ferrite and pearlite phases of the ASTM A36 steel specimens and the coefficient variation of its distribution calculated from the analysis are shown in Fig. 8. As we can see in the Fig. 8a, that the mean hardness of pearlite is higher than the ferrite for all the temperature exposures. The mean hardness of ferrite initially decreases when the exposed temperature increases till the exposed temperature is 700°C. But after 700°C, the mean hardness it shows a sharp increase and falls again at 1000°C. Interestingly, the variation of the pearlite exhibits the similar trend except for the sharp increase observed at 500°C The plot of coefficient of variation of hardness values presented in Fig. 8b indicates that the pearlite phase shows a wider variation of hardness values compared to the ferrite phase. The results showed that the mean hardness value of ferrite is ranged from 2.46 to 3.01 GPa, whereas the pearlite phase is ranged from 3.11 to 4.27 GPa for different temperature exposures. These nano-indentation hardness values are in agreement with the previous studies, and the comparison of these values with these existing studies is summarised in Table 1.

Similarly, the mean Young's modulus values of ferrite and pearlite phases and the coefficient variation of its distribution of different air-cooled ASTM A36 steel specimens are plotted and shown in Fig. 9. As we can see from Fig. 9a, the mean Young's moduli of ferrite phase is slightly lesser than that of pearlite's moduli at all the temperature exposures. Nevertheless, the differences in the mean Young's modulus between the two phases are found to be not statistically significant which and pearlite phase do not show any significant statistical differences between them which is in agreement with the existing literature (Freitas et al. 2009; Hutasoit et al. 2013; Li et al. 2019; Watanabe et al. 2011). However, the mean Young's modulus of ferrite is slightly lesser than that of pearlite's moduli. Also, the trend of the variation of mean Young's modulus with respect to the post-fire temperature of the ferrite phase is remarkably similar to that of the pearlite phase. The mean Young's moduli of ferrite range from 183.8 to 225.0 GPa, whereas the pearlite phase ranges from 195.8 to 231.2 GPa for different temperature exposures. The coefficient of variation of the distribution of Young's modulus values ranges from 0.031 to 0.047, which is significantly lesser than the variation range of nanoindentation hardness values which is 0.049 to 0.111.

To understand the nature of the distribution of both nanoindentation hardness and Young's modulus values, histograms, and Q-Q plots are constructed for both ferrite and pearlite phases separately for all the different elevated temperatures. Fig. 10-13 show histograms and Q-Q plots for ferrite and pearlite phases of steel specimens subjected to target temperatures of 27°C, 500°C, and 900°C. These plots indicate the distribution of nanoindentation hardness values roughly follow a normal distribution with pronounced deviations in the end quartiles. These deviations, though still present in the distribution of Young's modulus values, are less pronounced, and the normal distribution fits fairly well. The deviations from the normal distribution are more pronounced in the pearlite phase compared to the ferrite phase. This may be due to the fewer sampling points available in capturing the distribution.

5.2. Correlation of nano properties with macroscale properties of ASTM A36 steel

The relationship between nanoindentation hardness of ferrite and pearlite phases of ASTM A36 steels exposed to different elevated temperatures and their corresponding macroscale properties such as yield strength, tensile strength, and ductility were investigated. The macroscale properties were obtained from our previous study performed on the post-fire ASTM A36 steels [6]. The scattered plots between the nanoindentation hardness of the ferrite phase and the corresponding macroscale properties are provided in Fig. 14. These plots do not show any observable trends between the ferrite's nanoindentation hardness and any of the macroscale properties. The determined Pearson coefficient values for ferrite's nanoindentation hardness vs. yield strength, ferrite's nanoindentation hardness vs. tensile strength, and ferrite's nanoindentation hardness vs. ductility are 0.077, 0.291 and 0.021, respectively. These low correlation values further illustrate the lack of any correlation between the ferrite's nanoindentation hardness and any of the macroscale properties. Fig. 14 shows the scattered plots between the nanoindentation hardness of pearlite and the corresponding macroscale properties. The lack of linear association between the nanoindentation hardness and the macroscale properties are observed in these plots too. However, the relation between pearlite's nanoindentation hardness and yield strength and the relation between pearlite's nanoindentation hardness and tensile strength shows a nonlinear trend. When fitted with a quadratic regression curve, these two relations yielded an R-squared value of 0.76, which suggests the existence of a nonlinear relationship between nanoindentation hardness of pearlite and yield strength and between nanoindentation hardness of pearlite and tensile strength of the metal. The nonlinear relationships are given as follows,

$$YS = -290.8\overline{H}_p^2 + 2121.4\overline{H}_p - 3481.6 \tag{6}$$

$$TS = -205.2\overline{H}_p^2 + 1511.7\overline{H}_p - 2268.7 \tag{7}$$

where, YS and TS refers to the yield strength and tensile strength of post-fire steels, respectively and $\overline{H}_p$ refers to the mean hardness of pearlite.

In the case of multi-phase steels, the yield and ultimate strength are found to be strongly correlated to the volume fraction and properties of the harder phases like martensite in many studies (Choi et al. 2009; Srivastava et al. 2015; Wang et al. 2014). A strong correlation observed between the macroscopic yield and ultimate strength of ASTM A36 steel and the harder pearlite phase in this study confirms this trend reported in previously published literature. Furthermore, it is important to note that other popularly used structural steel grades like ASTM A572 and ASTM A992 also have ferrite-pearlite microstructure and hence the results obtained in this study can also be qualitatively extended to such steels [6, 47].

Ductility of structural steels will depend on the stress state and history, size, shape and distribution of material (Kiran and Khandelwal 2013; Kiran and Khandelwal 2014; Sajid and Kiran 2018) and surface defects in addition to the contrast in the metallurgical phase properties (Choi et al. 2009; Srivastava et al. 2015). With this, no strong correlation between ductility and metallurgical phase properties is expected. This trend is confirmed in the current study as observed in Fig. 14c and Fig. 15c where no significant correlation between hardness values of both ferrite and pearlite with macroscopic mechanical properties is observed. In this context, it is worthwhile to recall that the ductility of structural steels (ASTM A36, A572 and A992) is found not to depend on metallurgical phase volumes and grain sizes as noted in a previous study [6].

5. Conclusions

The important conclusions of this study are:

1. The phase compositions evaluated using the proposed nanoindentation and clustering technique revealed that the post-fire ASTM A36 steel specimens had 79% to 89% of ferrite and 11% to 21% of pearlite which is consistent with a previously published metallurgical study (Sajid et al. 2020).
2. The mean hardness of ferrite ranged from 2.46 to 3.01 GPa, while Young's modulus ranged from 183.8 to 225.0 GPa for different temperature exposures. On the other hand, the mean hardness of pearlite ranged from 3.11 to 4.27 GPa, while Young's modulus ranged from 195.8 to 231.2 GPa for different temperature exposures considered in this study. In other words, pearlite is harder and slightly stiffer when compared to ferrite in post-fire ASTM A36 steels. The nano properties of ferrite and pearlite in post-fire ASTM A36 are close to the ferrite and pearlite properties in other steels that are reported in the existing literature, which is summarized in Table 2.

3. The coefficient of variation of Young's modulus ranged from 0.031 to 0.047, which is significantly lesser than the variation range of nanoindentation hardness which is 0.049 to 0.111. The higher coefficient of variation of nanoindentation hardness might be due to the varying compositions of iron carbide present in pearlite colonies and the presence of ferrite-pearlite boundaries. Moreover, these factors did not contribute to a significant variation of Young's modulus because of the presence of iron carbides in pearlite (mixture of ferrite and iron carbides) does not alter the Youngs modulus of pearlite and the Youngs modulus of both ferrite and pearlite are numerically close.
4. Scattered plots drawn between the macroscale properties of the tested ASTM A36 steel specimens, namely yield strength, and tensile strength, and nanoindentation hardness indicated a quadratic correlation between the pearlite's mean nanoindentation hardness and the yield strength of different post-fire ASTM A36 steels. This quadratic correlation was also observed between pearlite's mean nanoindentation hardness and the tensile strength of the post-fire steel specimens.
5. No correlation between ferrite's nanoindentation hardness and the macroscale properties is observed. Furthermore, the ductility of the post-fire steel specimens does not show any correlation with the mean hardness of both ferrite and pearlite phases.
6. The proposed clustering of nanoindentation data can reveal the metallurgical phase compositions and nanoindentation properties simultaneously and hence can be a valuable tool to quantify the nano and macroscale property relationships.

Data Availability Statement

Some or all data, models, or code that support the findings of this study are available from the corresponding author upon reasonable request.

Acknowledgments

Research presented in this paper was supported by the National Science Foundation under NSF CAREER award # 2045538. Any opinions, findings, and conclusions, or recommendations expressed in this material are those of the author(s) and do not necessarily reflect the views of the National Science Foundation.

References

(1978). "Picture Thresholding Using an Iterative Selection Method." *IEEE Transactions on Systems, Man, and Cybernetics*, 8(8), 630-632.

(2013). "ASTM International, ASTM E112 Standard Test Methods for Determining Average Grain Size." ASTM International, West Conshohocken, PA.

Arthur, D., and Vassilvitskii, S. (2006). "k-means++: The advantages of careful seeding." Stanford.

Azhari, F., Heidarpour, A., Zhao, X.-L., and Hutchinson, C. R. (2015). "Mechanical properties of ultra-high strength (Grade 1200) steel tubes under cooling phase of a fire: an experimental investigation." *Construction and Building Materials*, 93, 841-850.

Aziz, E. M., and Kodur, V. K. (2016). "Effect of temperature and cooling regime on mechanical properties of high-strength low-alloy steel." *Fire and Materials*, 40(7), 926-939.

Bahr, D. F., Kramer, D. E., and Gerberich, W. W. (1998). "Non-linear deformation mechanisms during nanoindentation." *Acta Materialia*, 46(10), 3605-3617.

Baltazar Hernandez, V. H., Panda, S. K., Kuntz, M. L., and Zhou, Y. (2010). "Nanoindentation and microstructure analysis of resistance spot welded dual phase steel." *Materials Letters*, 64(2), 207-210.

Ban, H., Bai, R., Chung, K.-F., and Bai, Y. (2020). "Post-fire material properties of stainless-clad bimetallic steel." *Fire Safety Journal*, 112, 102964.

Bezdek, J. C., Ehrlich, R., and Full, W. (1984). "FCM: The fuzzy c-means clustering algorithm." *Computers & Geosciences*, 10(2), 191-203.

Campbell, L. (1967). *The Influence of Metallurgical Structure on the Mechanisms of Fatigue Crack Propagation*, ASTM International, West Conshohocken, PA.

Chen, J., Sand, K., Xia, M. S., Ophus, C., Mohammadi, R., Kuntz, M., Zhou, Y., and Mitlin, D. (2008). "Transmission electron microscopy and nanoindentation study of the weld zone microstructure of diode-laser-joined automotive transformation-induced plasticity steel." *Metallurgical and Materials Transactions A*, 39(3), 593-603.

Chen, Z., Lu, J., Liu, H., and Liao, X. (2016). "Experimental study on the post-fire mechanical properties of high-strength steel tie rods." *Journal of Constructional Steel Research*, 121, 311-329.

Chiew, S., Zhao, M., and Lee, C. (2014). "Mechanical properties of heat-treated high strength steel under fire/post-fire conditions." *Journal of Constructional Steel Research*, 98, 12-19.

Choi, K. S., Liu, W. N., Sun, X., and Khaleel, M. A. (2009). "Microstructure-based constitutive modeling of TRIP steel: Prediction of ductility and failure modes under different loading conditions." *Acta Materialia*, 57(8), 2592-2604.

Colwell, J. D., and Babic, D. (2012). "A Review of Oxidation on Steel Surfaces in the Context of Fire Investigations." *SAE Int. J. Passeng. Cars - Mech. Syst.*, 5(2), 1002-1015.

De Bono, D. M., London, T., Baker, M., and Whiting, M. J. (2017). "A robust inverse analysis method to estimate the local tensile properties of heterogeneous materials from nano-indentation data." *International Journal of Mechanical Sciences*, 123, 162-176.

Debehets, J., Tacq, J., Favache, A., Jacques, P., Seo, J. W., Verlinden, B., and Seefeldt, M. (2014). "Analysis of the variation in nanohardness of pearlitic steel: Influence of the interplay between ferrite crystal orientation and cementite morphology." *Materials Science and Engineering: A*, 616, 99-106.

Defays, D. (1977). "An efficient algorithm for a complete link method." *The Computer Journal*, 20(4), 364-366.

Ding, F., Zhang, C., Yu, Y., Lan, L., and Man, M. (2019). "Hysteretic behavior of post fire structural steels under cyclic loading." *Journal of Constructional Steel Research*, 105847.

Elwazri, A. M., Wanjara, P., and Yue, S. (2005). "The effect of microstructural characteristics of pearlite on the mechanical properties of hypereutectoid steel." *Materials Science and Engineering: A*, 404(1), 91-98.

Ester, M., Kriegel, H. P., Sander, J., and Xiaowei, X. (Sponsor Org.:). "A density-based algorithm for discovering clusters in large spatial databases with noise." AAAI Press, Menlo Park, CA (United States), Research Org.:.

Everitt, B., Landau, S., and Leese, M. (2001). *Cluster analysis*, Arnold Press, London.

Freitas, V. L. D. A., Silva, A. A., Silva, E. D. M., De Albuquerque, V. H. C., and Tavares, J. M. R. (2009). "Microstructural characterization of carbon steels using ultrasonic velocity measurements."

Gadelrab, K. R., Li, G., Chiesa, M., and Souier, T. (2012). "Local characterization of austenite and ferrite phases in duplex stainless steel using MFM and nanoindentation." *Journal of Materials Research*, 27(12), 1573-1579.

Gain, A. K., and Zhang, L. (2020). "Nanoindentation Creep, Elastic Properties, and Shear Strength Correlated with the Structure of Sn-9Zn-0.5nano-Ag Alloy for Advanced Green Electronics." *Metals*, 10(9), 1137.

Griffiths, A., Robinson, L. A., and Willett, P. (1984). "Hierarchic agglomerative clustering methods for automatic document classification." *Journal of Documentation*.

Gunalan, S., and Mahendran, M. (2014). "Experimental investigation of post-fire mechanical properties of cold-formed steels." *Thin-Walled Structures*, 84, 241-254.

Hutasoit, N., Yan, W., Cottam, R., Brandt, M., and Blicblau, A. (2013). "Evaluation of microstructure and mechanical properties at the interface region of laser-clad Stellite 6 on steel using nanoindentation." *Metallography, Microstructure, and Analysis*, 2(5), 328-336.

Igwemezie, V. C., Ugwuegbu, C. C., and Mark, U. (2016). "Physical Metallurgy of Modern Creep-Resistant Steel for Steam Power Plants: Microstructure and Phase Transformations." *Journal of Metallurgy*, 2016, 5468292.

Jiang, Z., Guan, Z., and Lian, J. (1995). "Effects of microstructural variables on the deformation behaviour of dual-phase steel." *Materials Science and Engineering: A*, 190(1), 55-64.

Kamaya, M. (2009). "Characterization of microstructural damage due to low-cycle fatigue by EBSD observation." *Materials Characterization*, 60(12), 1454-1462.

Kang, L., Suzuki, M., Ge, H., and Wu, B. (2018). "Experiment of ductile fracture performances of HSSS Q690 after a fire." *Journal of Constructional Steel Research*, 146, 109-121.

Kiran, R., and Khandelwal, K. (2013). "A micromechanical model for ductile fracture prediction in ASTM A992 steels." *Engineering Fracture Mechanics*, 101, 102-117.

Kiran, R., and Khandelwal, K. (2014). "A Triaxiality and Lode Parameter Dependent Ductile Fracture Criterion." *Engineering Fracture Mechanics*, Vol. 128, 121-138.

Krauss, G. (2015). *Steels: Processing, Structure, and Performance*, ASM International, Materials Park, Ohio.

Kriegel, H.-P., Kröger, P., Sander, J., and Zimek, A. (2011). "Density-based clustering." *WIREs Data Mining and Knowledge Discovery*, 1(3), 231-240.

Kumar, A., Singh, S. B., and Ray, K. K. (2008). "Influence of bainite/martensite-content on the tensile properties of low carbon dual-phase steels." *Materials Science and Engineering: A*, 474(1), 270-282.

Lee, J., Engelhardt, M. D., and Taleff, E. M. (2012). "Mechanical Properties of ASTM A 992 Steel After Fire." *Engineering Journal(Chicago)*, 49(1), 33-44.

Leng, Y. (2009). *Materials characterization: introduction to microscopic and spectroscopic methods*, John Wiley & Sons.

Li, C., Zhao, H., Sun, L., and Yu, X. (2019). "In situ nanoindentation method for characterizing tensile properties of AISI 1045 steel based on mesomechanical analysis." *Advances in Mechanical Engineering*, 11(7), 1687814019862919.

Li, G.-Q., Lyu, H., and Zhang, C. (2017). "Post-fire mechanical properties of high strength Q690 structural steel." *Journal of Constructional Steel Research*, 132, 108-116.

Li, Y., and Wu, H. (2012). "A Clustering Method Based on K-Means Algorithm." *Physics Procedia*, 25, 1104-1109.

Li, Z., Kiran, R., Hu, J., Hector, L. G., and Bower, A. F. (2020). "Analysis and design of a three-phase TRIP steel microstructure for enhanced fracture resistance." *International Journal of Fracture*, 221(1), 53-85.

Liu, M., Lu, C., Tieu, K., and Yu, H. (2014). "Numerical comparison between Berkovich and conical nano-indentations: Mechanical behaviour and micro-texture evolution." *Materials Science and Engineering: A*, 619, 57-65.

Lloyd, S. (1982). "Least squares quantization in PCM." *IEEE Transactions on Information Theory*, 28(2), 129-137.

Lu, J., Liu, H., Chen, Z., and Bisby, L. (2017). "Experimental investigation of the residual mechanical properties of cast steels after exposure to elevated temperature." *Construction and Building Materials*, 143, 259-271.

Lu, J., Liu, H., Chen, Z., and Liao, X. (2016). "Experimental investigation into the post-fire mechanical properties of hot-rolled and cold-formed steels." *Journal of Constructional Steel Research*, 121, 291-310.

MacQueen, J. "Some methods for classification and analysis of multivariate observations." *Proc., Proceedings of the fifth Berkeley symposium on mathematical statistics and probability*, Oakland, CA, USA, 281-297.

Mann, A. B. (2005). "9 - Nanoindentation." *Surfaces and Interfaces for Biomaterials*, P. Vadgama, ed., Woodhead Publishing, 225-247.

Mazaheri, Y., Kermanpur, A., and Najafizadeh, A. (2015). "Nanoindentation study of ferrite–martensite dual phase steels developed by a new thermomechanical processing." *Materials Science and Engineering: A*, 639, 8-14.

Menčík, J., Munz, D., Quandt, E., Weppelmann, E. R., and Swain, M. V. (1997). "Determination of elastic modulus of thin layers using nanoindentation." *Journal of Materials Research*, 12(9), 2475-2484.

Naik, D. L., Sajid, H. U., and Kiran, R. (2019). "Texture-Based Metallurgical Phase Identification in Structural Steels: A Supervised Machine Learning Approach." *Metals*, 9(5), 546.

Nguyen, N.-V., Pham, T.-H., and Kim, S.-E. (2018). "Characterization of strain rate effects on the plastic properties of structural steel using nanoindentation." *Construction and Building Materials*, 163, 305-314.

Oliver, W. C., and Pharr, G. M. (1992). "An improved technique for determining hardness and elastic modulus using load and displacement sensing indentation experiments." *Journal of Materials Research*, 7(6), 1564-1583.

Ostrovsky, R., Rabani, Y., Schulman, L. J., and Swamy, C. "The Effectiveness of Lloyd-Type Methods for the k-Means Problem." *Proc., 2006 47th Annual IEEE Symposium on Foundations of Computer Science (FOCS'06)*, 165-176.

Outinen, J., and Mäkeläinen, P. (2004). "Mechanical properties of structural steel at elevated temperatures and after cooling down." *Fire and materials*, 28(2-4), 237-251.

Pham, T.-H., Kim, J. J., and Kim, S.-E. (2014). "Estimation of microstructural compositions in the weld zone of structural steel using nanoindentation." *Journal of Constructional Steel Research*, 99, 121-128.

Pham, T.-H., and Kim, S.-E. (2015). "Nanoindentation for investigation of microstructural compositions in SM490 steel weld zone." *Journal of Constructional Steel Research*, 110, 40-47.

Pham, T.-H., and Kim, S.-E. (2017). "Characteristics of microstructural phases relevant to the mechanical properties in structural steel weld zone studied by using indentation." *Construction and Building Materials*, 155, 176-186.

Pham, T.-H., and Nguyen, N.-V. (2021). "Mechanical properties of constituent phases in structural steels and heat-affected zones investigated by statistical nanoindentation analysis." *Construction and Building Materials*, 268, 121211.

Qiang, X., Bijlaard, F. S., and Kolstein, H. (2012). "Post-fire mechanical properties of high strength structural steels S460 and S690." *Engineering Structures*, 35, 1-10.

Qiang, X., Bijlaard, F. S., and Kolstein, H. (2013). "Post-fire performance of very high strength steel S960." *Journal of Constructional Steel Research*, 80, 235-242.

Ren, C., Dai, L., Huang, Y., and He, W. (2020). "Experimental investigation of post-fire mechanical properties of Q235 cold-formed steel." *Thin-Walled Structures*, 150, 106651.

Rui, X., and Wunsch, D. (2005). "Survey of clustering algorithms." *IEEE Transactions on Neural Networks*, 16(3), 645-678.

Sagadevan, S., and Murugasen, P. (2014). "Novel Analysis on the Influence of Tip Radius and Shape of the Nanoindenter on the Hardness of Materials." *Procedia Materials Science*, 6, 1871-1878.

Sajid, H. U., and Kiran, R. (2018). "Influence of high stress triaxiality on mechanical strength of ASTM A36, ASTM A572 and ASTM A992 steels." *Construction and Building Materials*, 176, 129-134.

Sajid, H. U., and Kiran, R. (2018). "Influence of stress concentration and cooling methods on post-fire mechanical behavior of ASTM A36 steels." *Construction and Building Materials*, 186, 920-945.

Sajid, H. U., and Kiran, R. (2019). "Post-fire mechanical behavior of ASTM A572 steels subjected to high stress triaxialities." *Engineering Structures*, 191, 323-342.

Sajid, H. U., Naik, D. L., and Kiran, R. (2020). "Microstructure–Mechanical Property Relationships for Post-Fire Structural Steels." *Journal of Materials in Civil Engineering*, 32(6), 04020133.

Sander, J., Ester, M., Kriegel, H.-P., and Xu, X. (1998). "Density-Based Clustering in Spatial Databases: The Algorithm GDBSCAN and Its Applications." *Data Mining and Knowledge Discovery*, 2(2), 169-194.

Schuh, C. A. (2006). "Nanoindentation studies of materials." *Materials Today*, 9(5), 32-40.

Schwarm, S. C., Kolli, R. P., Aydogan, E., Mburu, S., and Ankem, S. (2017). "Characterization of phase properties and deformation in ferritic-austenitic duplex stainless steels by nanoindentation and finite element method." *Materials Science and Engineering: A*, 680, 359-367.

Schwartz, A. J., Kumar, M., Adams, B. L., and Field, D. P. (2009). *Electron backscatter diffraction in materials science*, Springer.

Shen, Y.-L. (2019). "Nanoindentation for Testing Material Properties." *Handbook of Mechanics of Materials*, S. Schmauder, C.-S. Chen, K. K. Chawla, N. Chawla, W. Chen, and Y. Kagawa, eds., Springer Singapore, Singapore, 1981-2012.

Sibson, R. (1973). "SLINK: An optimally efficient algorithm for the single-link cluster method." *The Computer Journal*, 16(1), 30-34.

Siwei, C., Shaokun, J., Houzuo, G., Huixuan, C., Yifeng, L., and Kang, L. (2017). "Mechanical and ductile fracture performances of high strength structural steel Q690 after a fire: experimental investigation." *Procedia Engineering*, 210, 496-503.

Smith, C. I., Kirby, B. R., Lapwood, D. G., Cole, K. J., Cunningham, A. P., and Preston, R. R. (1981). "The reinstatement of fire damaged steel framed structures." *Fire Safety Journal*, 4(1), 21-62.

Srivastava, A., Ghassemi-Armaki, H., Sung, H., Chen, P., Kumar, S., and Bower, A. F. (2015). "Micromechanics of plastic deformation and phase transformation in a three-phase TRIP-assisted advanced high strength steel: Experiments and modeling." *Journal of the Mechanics and Physics of Solids*, 78, 46-69.

Tao, Z., Wang, X.-Q., Hassan, M. K., Song, T.-Y., and Xie, L.-A. (2018). "Behaviour of three types of stainless steel after exposure to elevated temperatures." *Journal of Constructional Steel Research*.

Tatar, J. (2021). "Nanomechanical properties of cement Paste-Epoxy interphase following hygrothermal conditioning by water immersion." *Construction and Building Materials*, 282, 122695.

Tatar, J., Taylor, C. R., and Hamilton, H. R. (2019). "A multiscale micromechanical model of adhesive interphase between cement paste and epoxy supported by nanomechanical evidence." *Composites Part B: Engineering*, 172, 679-689.

Taylor, M. D., Choi, K. S., Sun, X., Matlock, D. K., Packard, C. E., Xu, L., and Barlat, F. (2014). "Correlations between nanoindentation hardness and macroscopic mechanical properties in DP980 steels." *Materials Science and Engineering: A*, 597, 431-439.

Tsui, T. Y., Oliver, W. C., and Pharr, G. M. (1996). "Influences of stress on the measurement of mechanical properties using nanoindentation: Part I. Experimental studies in an aluminum alloy." *Journal of Materials Research*, 11(3), 752-759.

Tuninetti, V., Jaramillo, A. F., Riu, G., Rojas-Ulloa, C., Znaidi, A., Medina, C., Mateo, A. M., and Roa, J. J. (2021). "Experimental Correlation of Mechanical Properties of the Ti-6Al-4V Alloy at Different Length Scales." *Metals*, 11(1), 104.

Wang, C., Ding, H., Cai, M., and Rolfe, B. (2014). "Multi-phase microstructure design of a novel high strength TRIP steel through experimental methodology." *Materials Science and Engineering: A*, 610, 436-444.

Wang, F., and Lui, E. M. (2020). "Experimental study of the post-fire mechanical properties of Q690 high strength steel." *Journal of Constructional Steel Research*, 167, 105966.

Wang, W., Liu, T., and Liu, J. (2015). "Experimental study on post-fire mechanical properties of high strength Q460 steel." *Journal of Constructional Steel Research*, 114, 100-109.

Watanabe, I., Setoyama, D., and Iwata, N. "Multi-scale modelling for ferrite-pearlite composite steel." *Proc., COMPLAS XI: proceedings of the XI International Conference on Computational Plasticity: fundamentals and applications*, CIMNE, 630-641.

Yan, X., Xia, Y., Blum, H. B., and Gernay, T. (2021). "Post-fire mechanical properties of advanced high-strength cold-formed steel alloys." *Thin-Walled Structures*, 159, 107293.

Zhang, C., Wang, R., and Song, G. (2020). "Post-fire mechanical properties of Q460 and Q690 high strength steels after fire-fighting foam cooling." *Thin-Walled Structures*, 156, 106983.

Zhu, M.-L., and Xuan, F.-Z. (2010). "Correlation between microstructure, hardness and strength in HAZ of dissimilar welds of rotor steels." *Materials Science and Engineering: A*, 527(16-17), 4035-4042.

Zhu, Y., Huang, S., and Sajid, H. U. (2021). "Micro-Mechanisms and Modeling of Ductile Fracture Initiation in Structural Steel after Exposure to Elevated Temperatures." *Metals*, 11(5), 767.

Figures

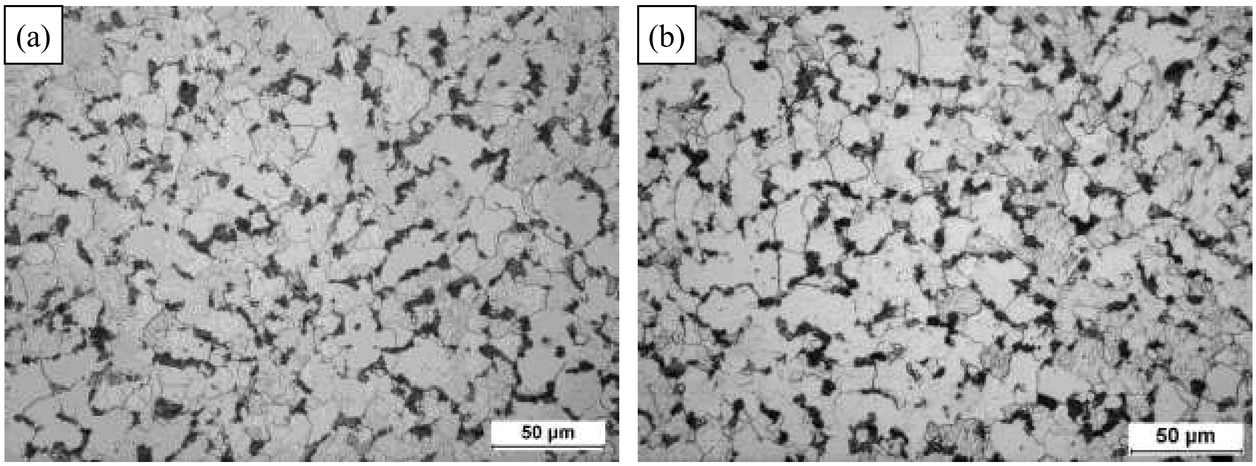

Fig. 1: Microstructures of ASTM A36 steel obtained at (a) room temperature, and (b) air-cooled from 500°C (dark regions: pearlite, light grey regions: ferrite) obtained using inverted metallurgical microscope.

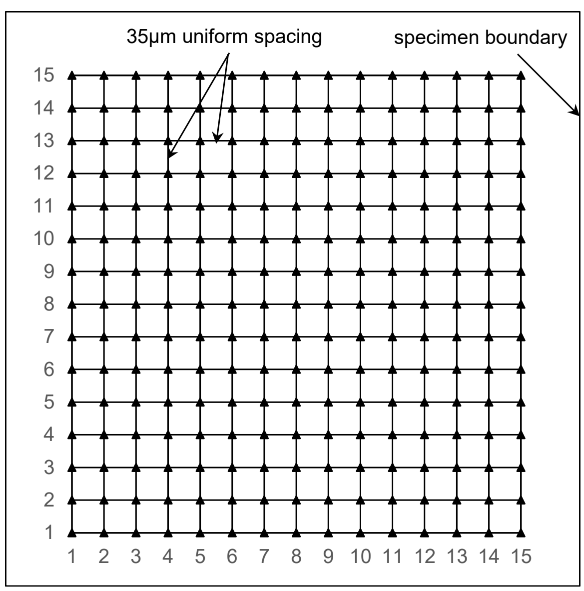

Fig. 2: A layout of nanoindentations performed on ASTM A36 specimens. The layout consists of 15×15 grid points with a spacing of 35μm in both directions. In total, 225 nanoindentations performed on each specimen.

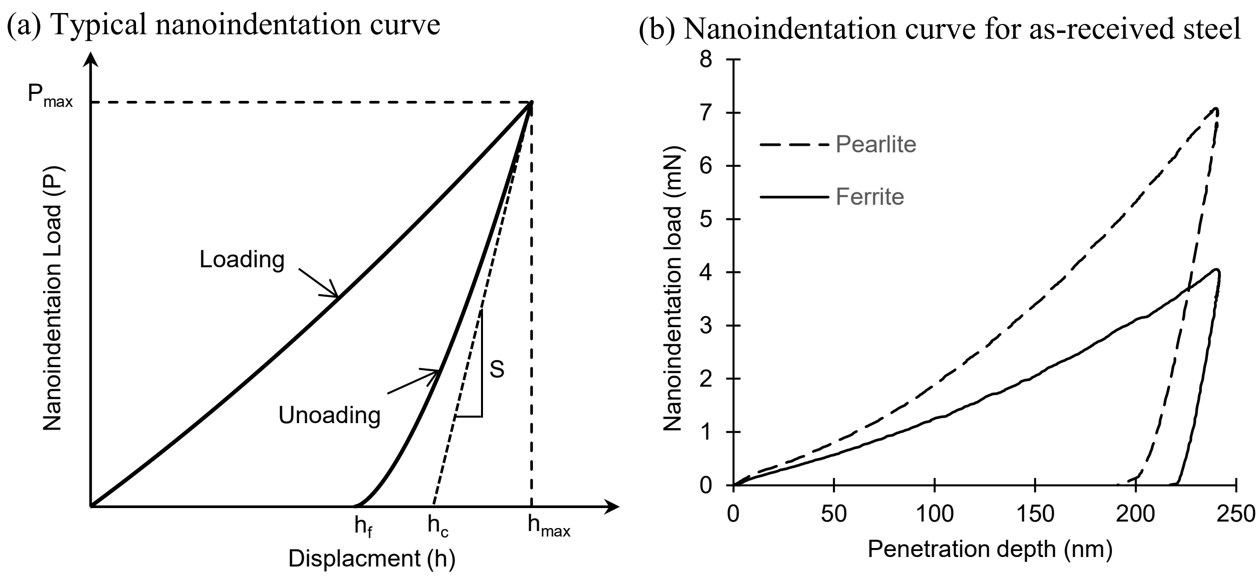

Fig. 3: a) Typical relationship between nanoindentation load and displacement of penetration depth of the indenter, b) Nanoindentation curve obtained in the current study for as-received ASTM A36 steel specimen.

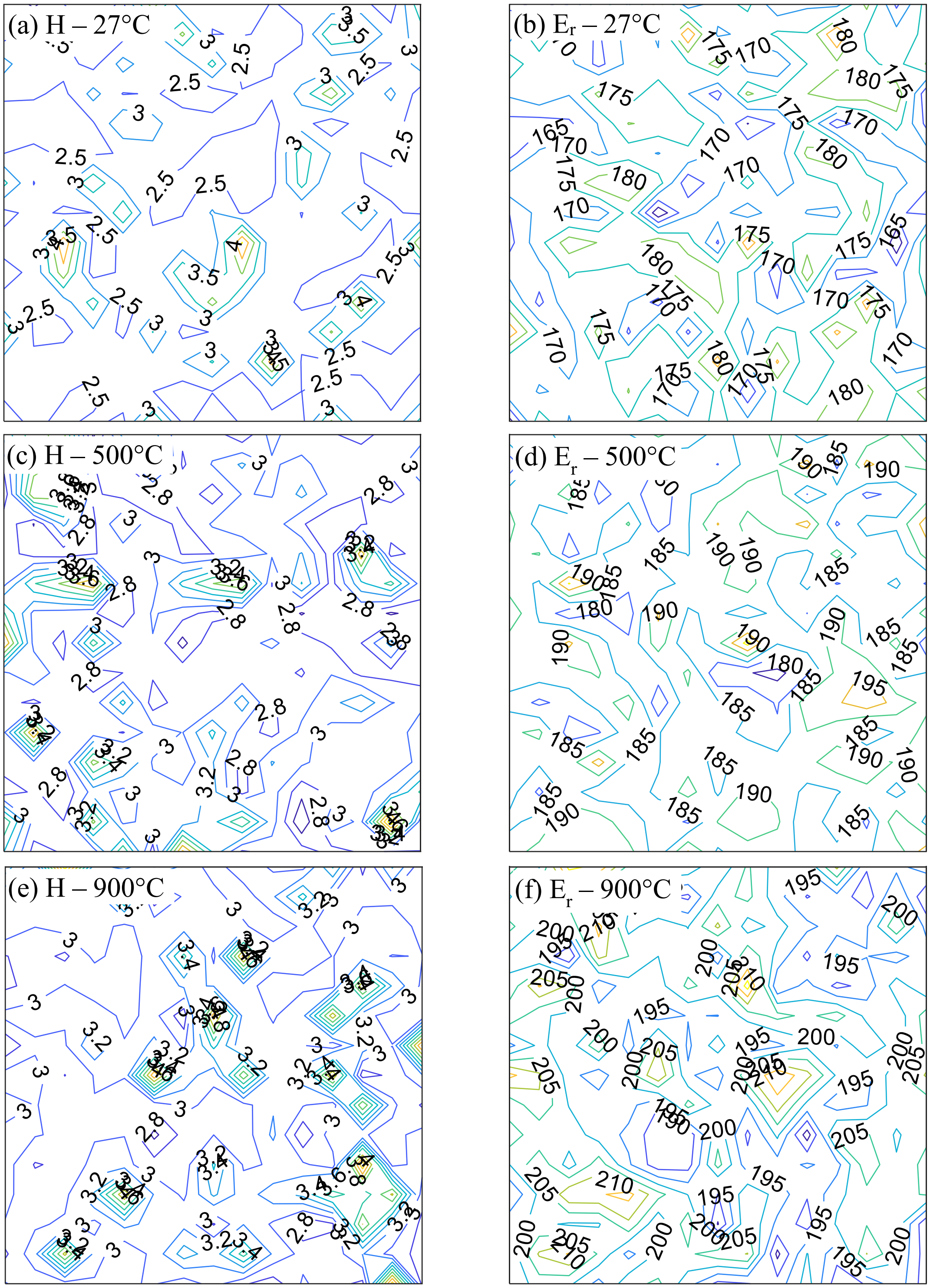

Fig. 4: Contour maps of nanoindentation values – hardness (H), GPa and reduced Young's modulus (E_r), GPa – of A36 steel a & b) as received, air cooled from c & d) 500°C and e & f) 900°C.

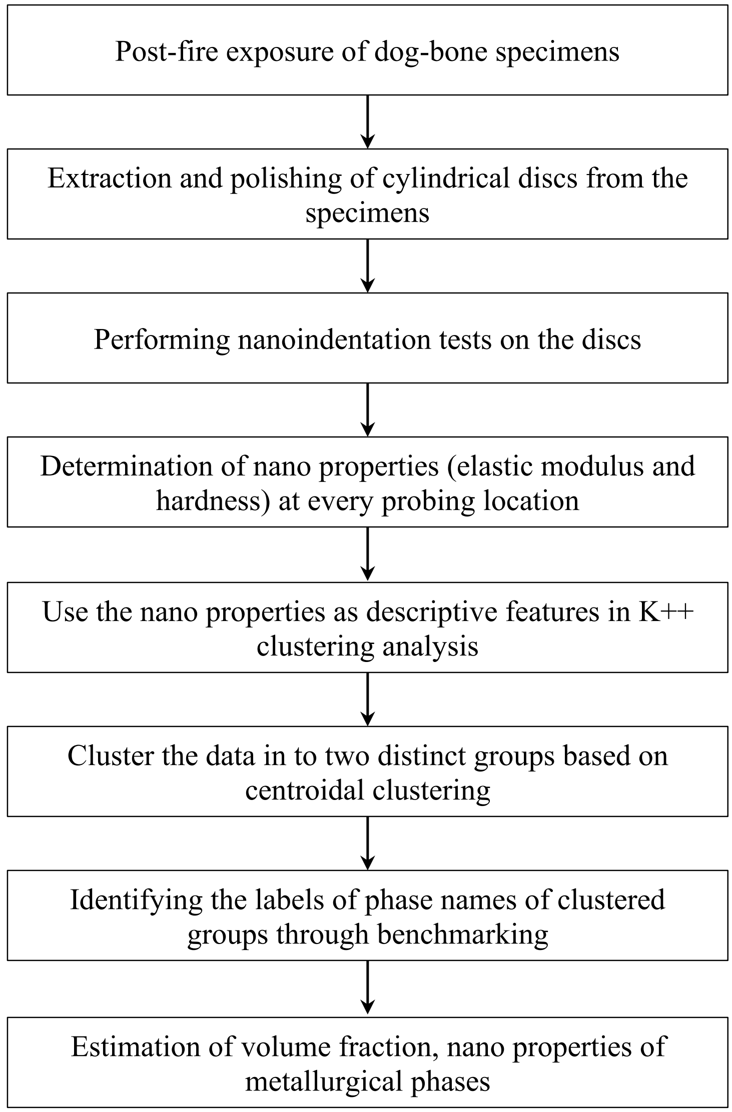

Fig. 5: Flow chart of the research methodology employed in this study

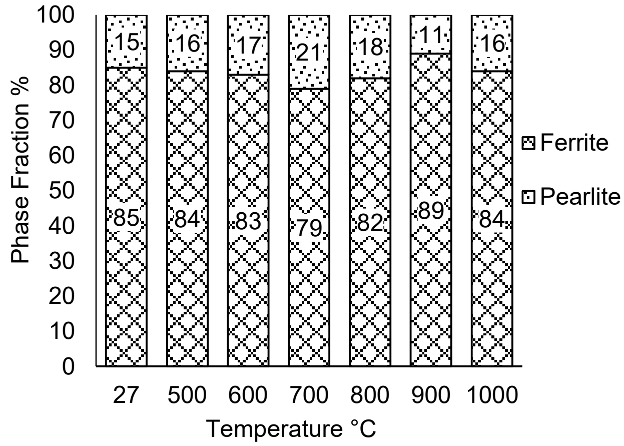

Fig. 6: Prediction of volume fraction of ferrite and pearlite metallurgical phases in post-fire A36 steel using K-means++ clustering on nanoindentation data.

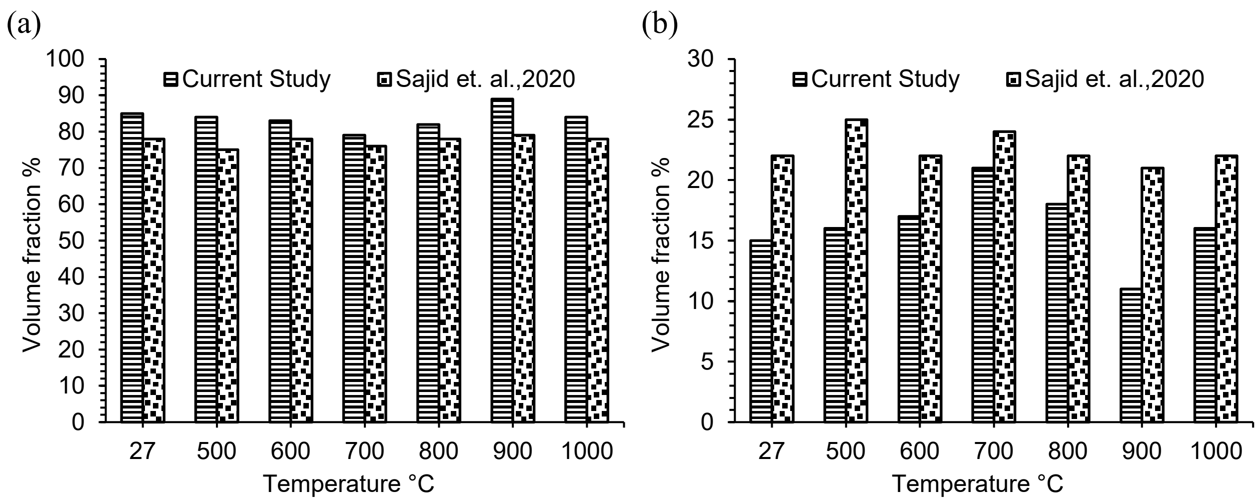

Fig. 7: Comparison of volume fraction of (a) ferrite and (b) pearlite metallurgical phases in post-fire A36 steel using K-means++ clustering on nanoindentation data with the reference literature (Sajid et. al.,2020(Sajid et al. 2020)).

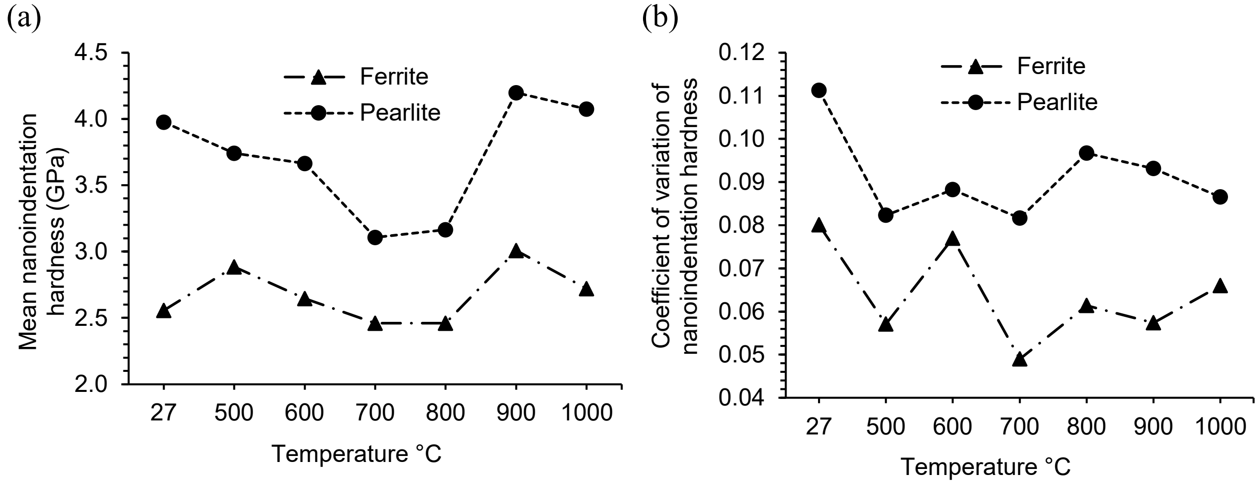

Fig. 8: (a) Mean nanoindentation hardness and (b) coefficient of variation of nanoindentation hardness of ferrite and pearlite phases predicted by clustering techniques for ASTM A36 steel specimens air-cooled from various elevated temperatures.

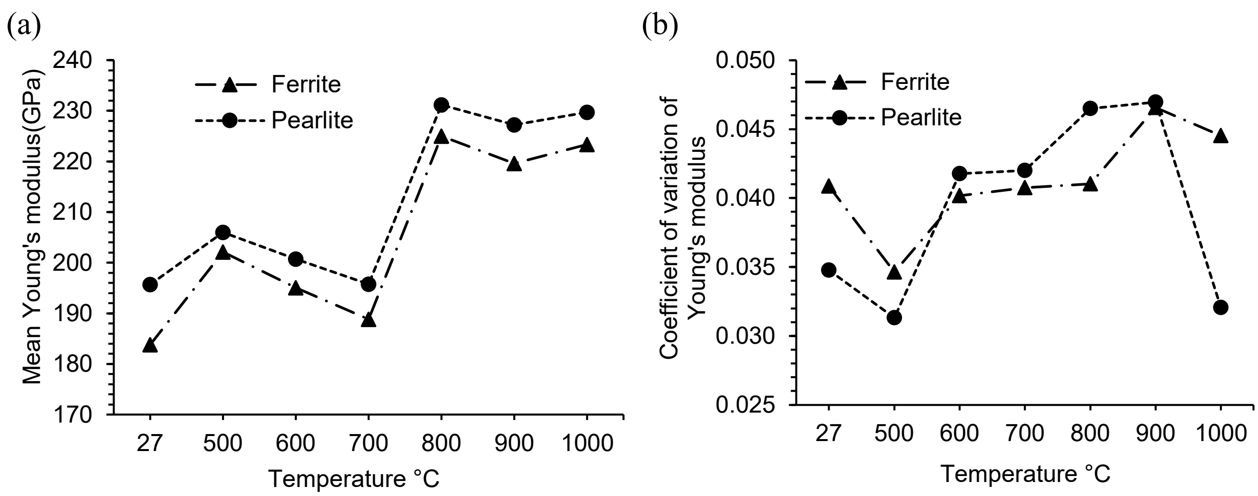

Fig. 9: (a) Mean Young's modulus and (b) coefficient of variation of Young's modulus of ferrite and pearlite phases predicted by clustering techniques for ASTM A36 steel specimens air-cooled from various elevated temperature.

(a) AC-27°C: Ferrite

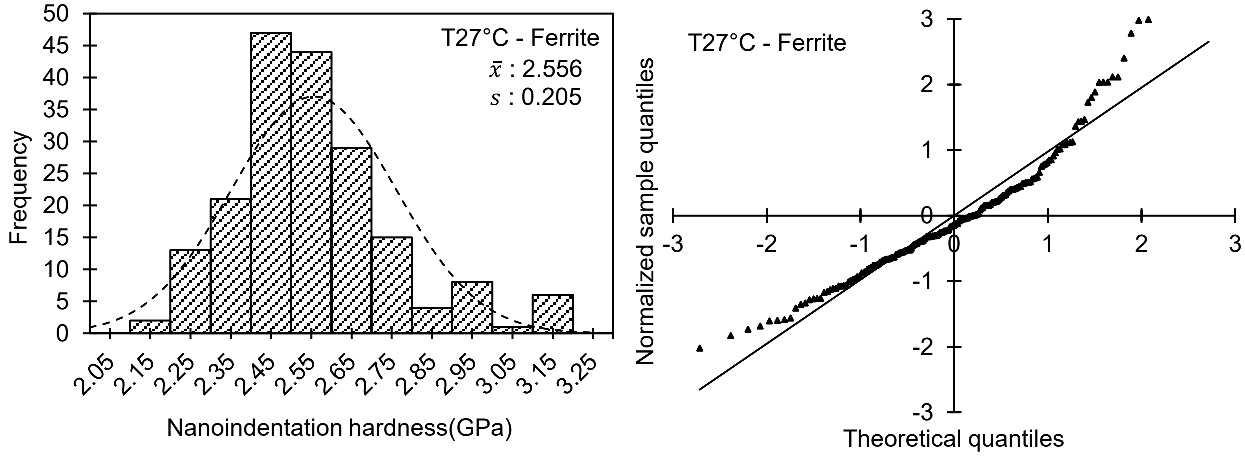

(b) AC-500°C: Ferrite

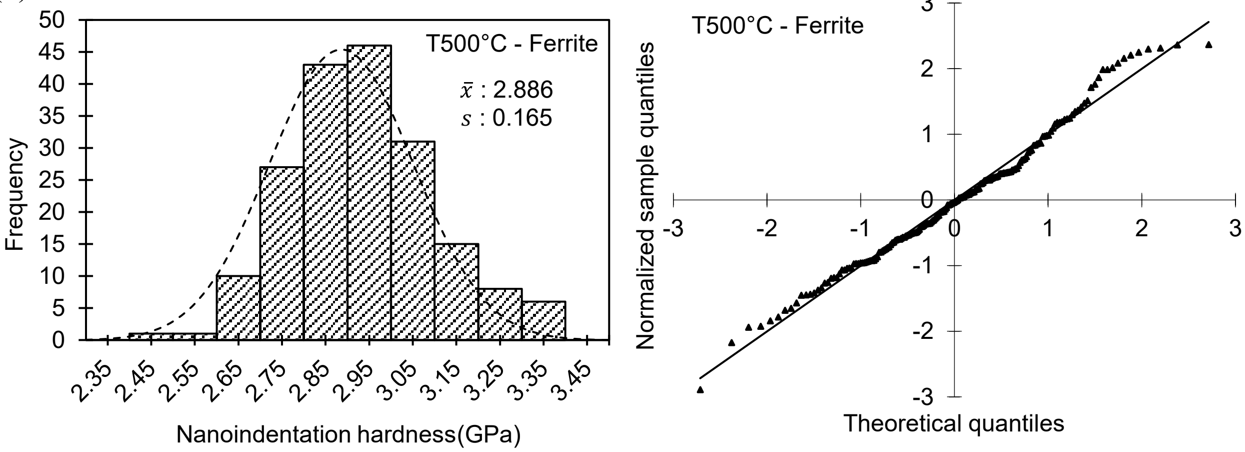

(c) AC-900°C: Ferrite

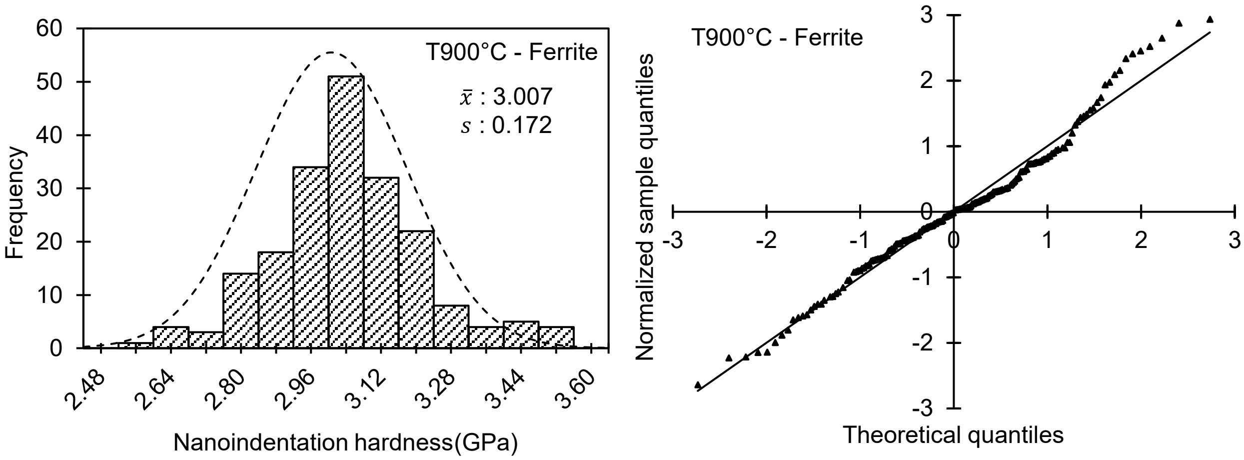

Fig. 10: Histogram and Q-Q plot of nanoindentation hardness of ferrite phase for A36 steel a) as received, air-cooled from b) 500° and c) 900°C. The probability plot shows the hardness values are almost distributed normally. The mean hardness value of ferrite ranges from 2.46 to 3.01 GPa and the coefficient of variation ranges from 0.049 to 0.080.

(a) AC-27°C: Pearlite

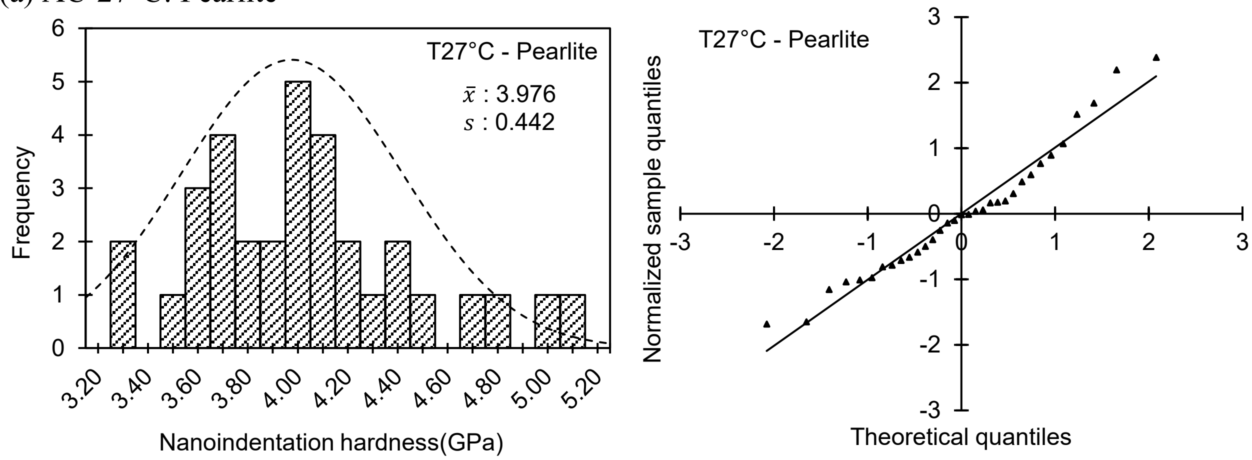

(b) AC-500°C: Pearlite

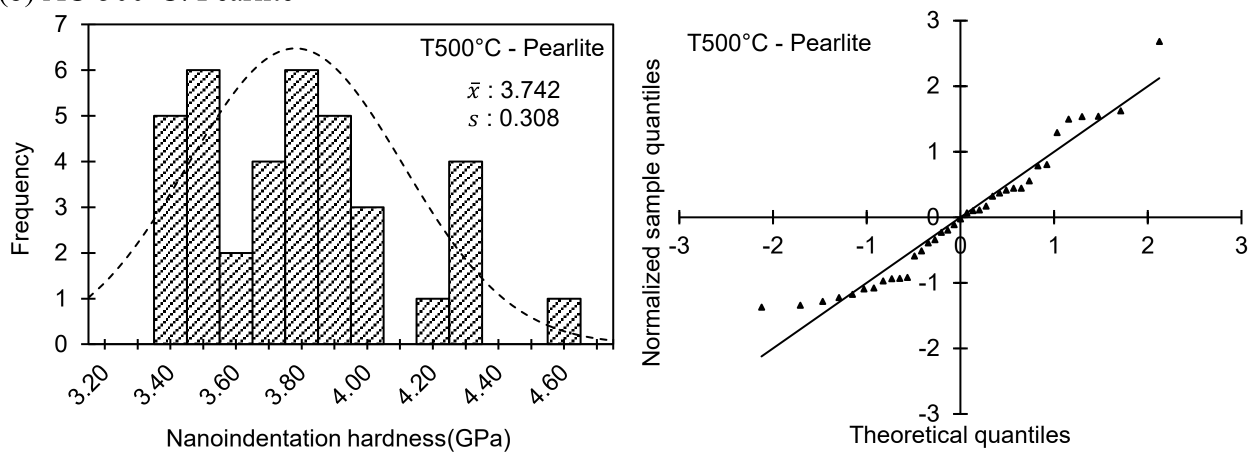

(c) AC-900°C: Pearlite

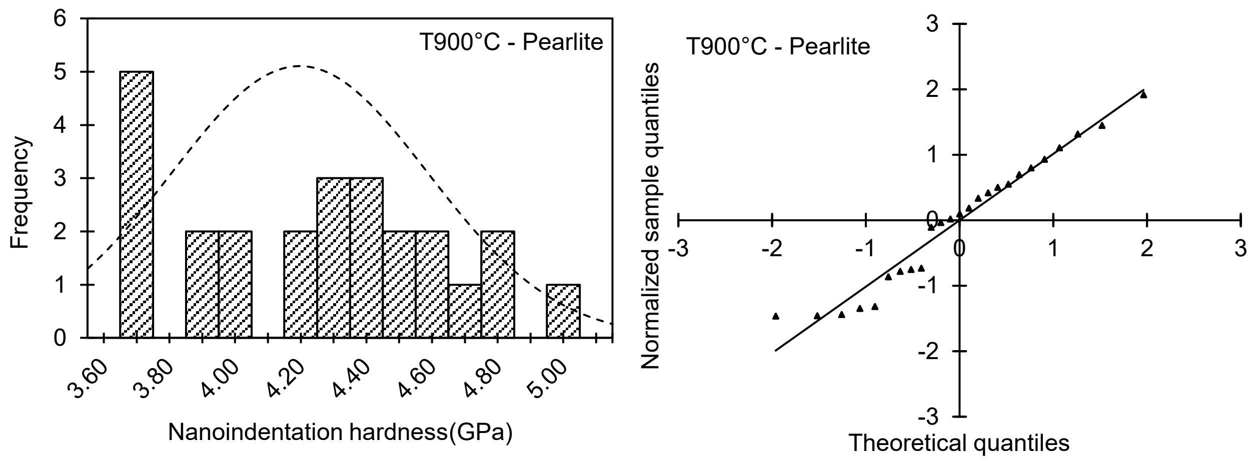

Fig. 11: Histogram and probability plot of nanoindentation hardness of pearlite phase for A36 steel at a) as received, air-cooled from b) 500°C and c) 900°C. The mean hardness value of pearlite ranges from 3.11 to 4.20 GPa and the coefficient of variation ranges from 0.082 to 0.111.

(a) AC-27°C: Ferrite

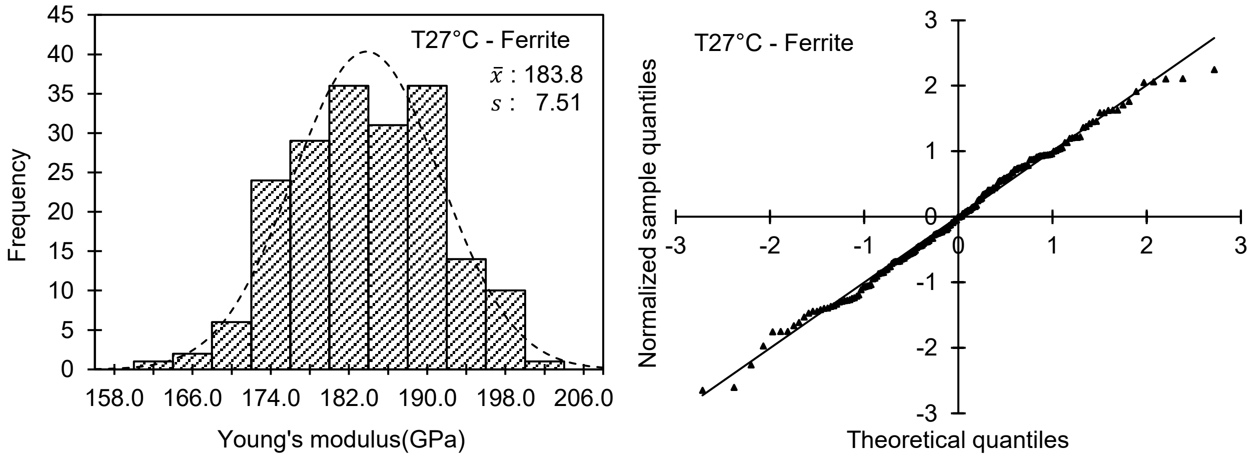

(b) AC-500°C: Ferrite

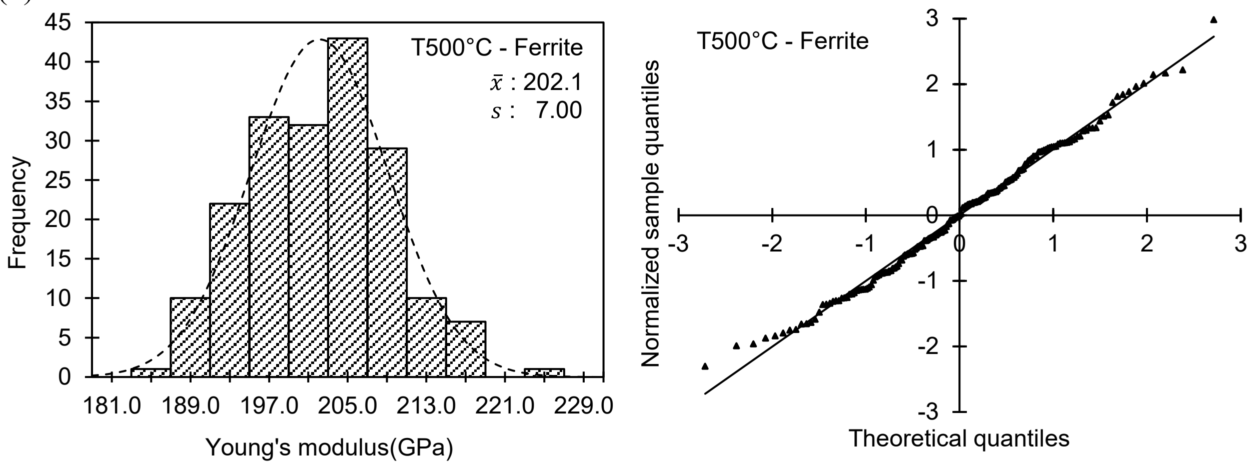

(c) AC-900°C: Ferrite

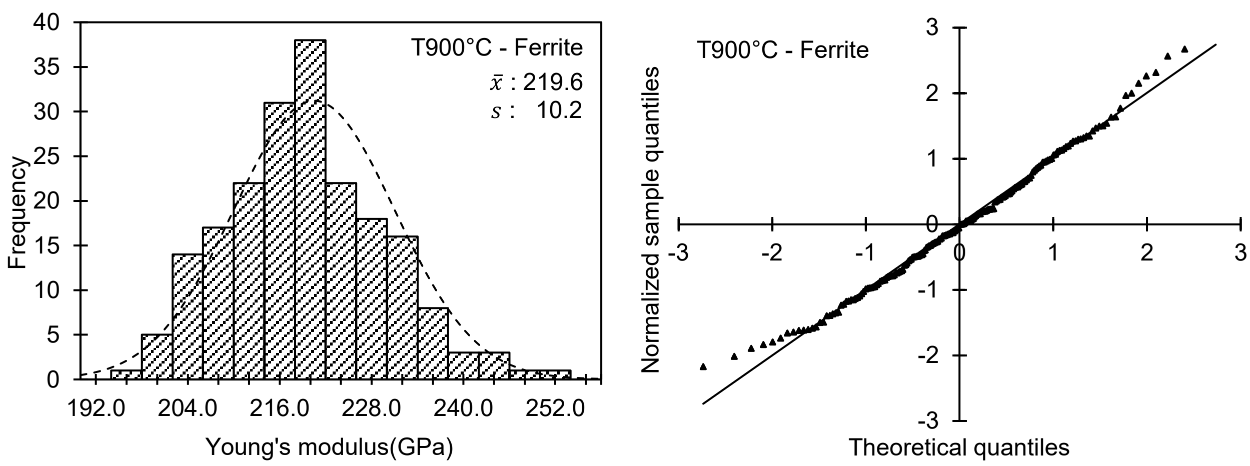

Fig. 12: Histogram and Q-Q plot of Young's modulus of ferrite phase for A36 steel a) as received, air-cooled from b) 500° and c) 900°C. The probability plot shows the hardness values are almost distributed normally. The mean hardness value of ferrite ranges from 183.8 to 225.0 GPa and the coefficient of variation ranges from 0.035 to 0.047.

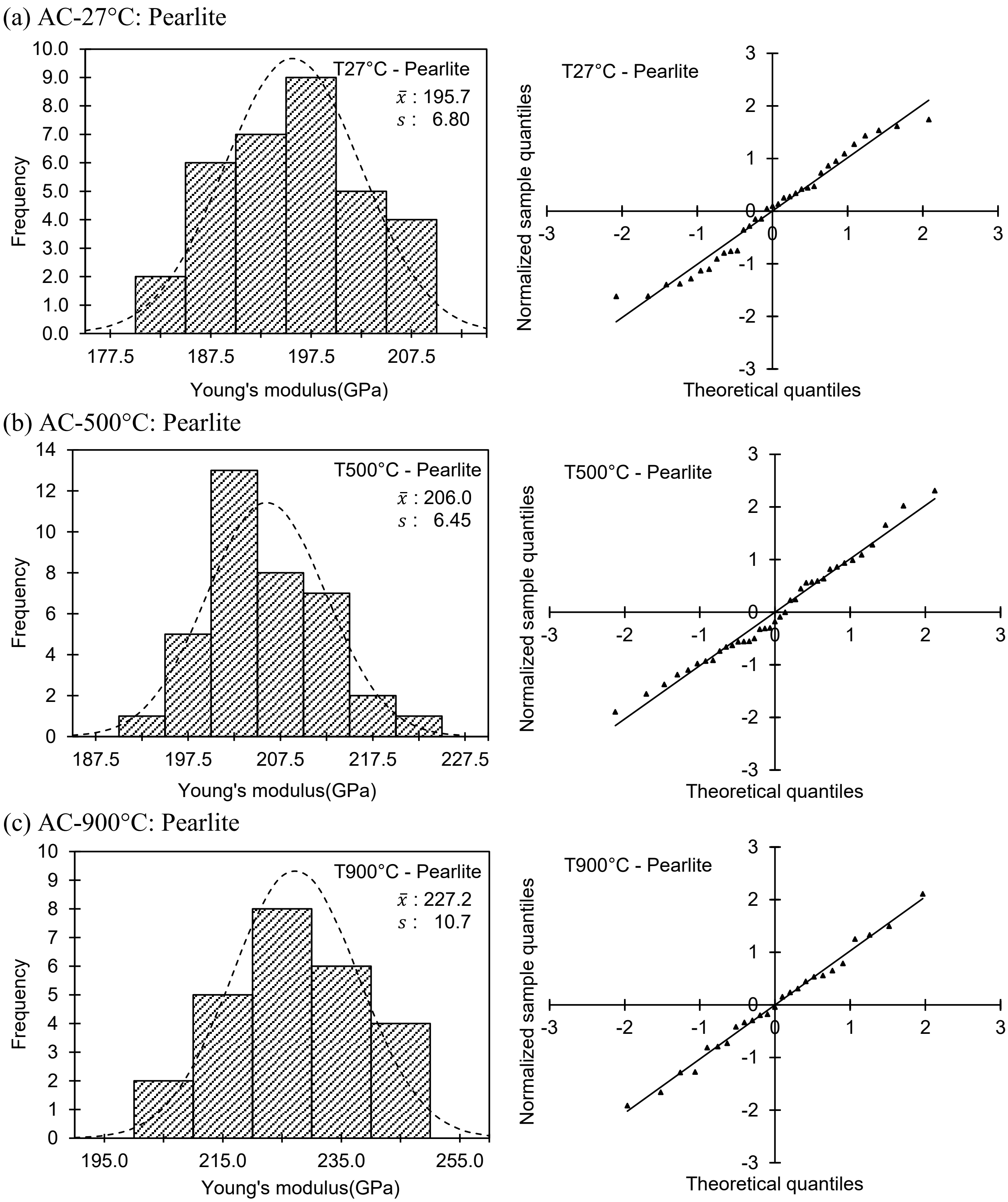

Fig. 13: Histogram and probability plot of Young's modulus of pearlite phase for A36 steel at a) as received, air-cooled from b) 500°C and c) 900°C. The mean hardness value of pearlite ranges from 195.8 to 231.2 GPa and the coefficient of variation ranges from 0.031 to 0.047

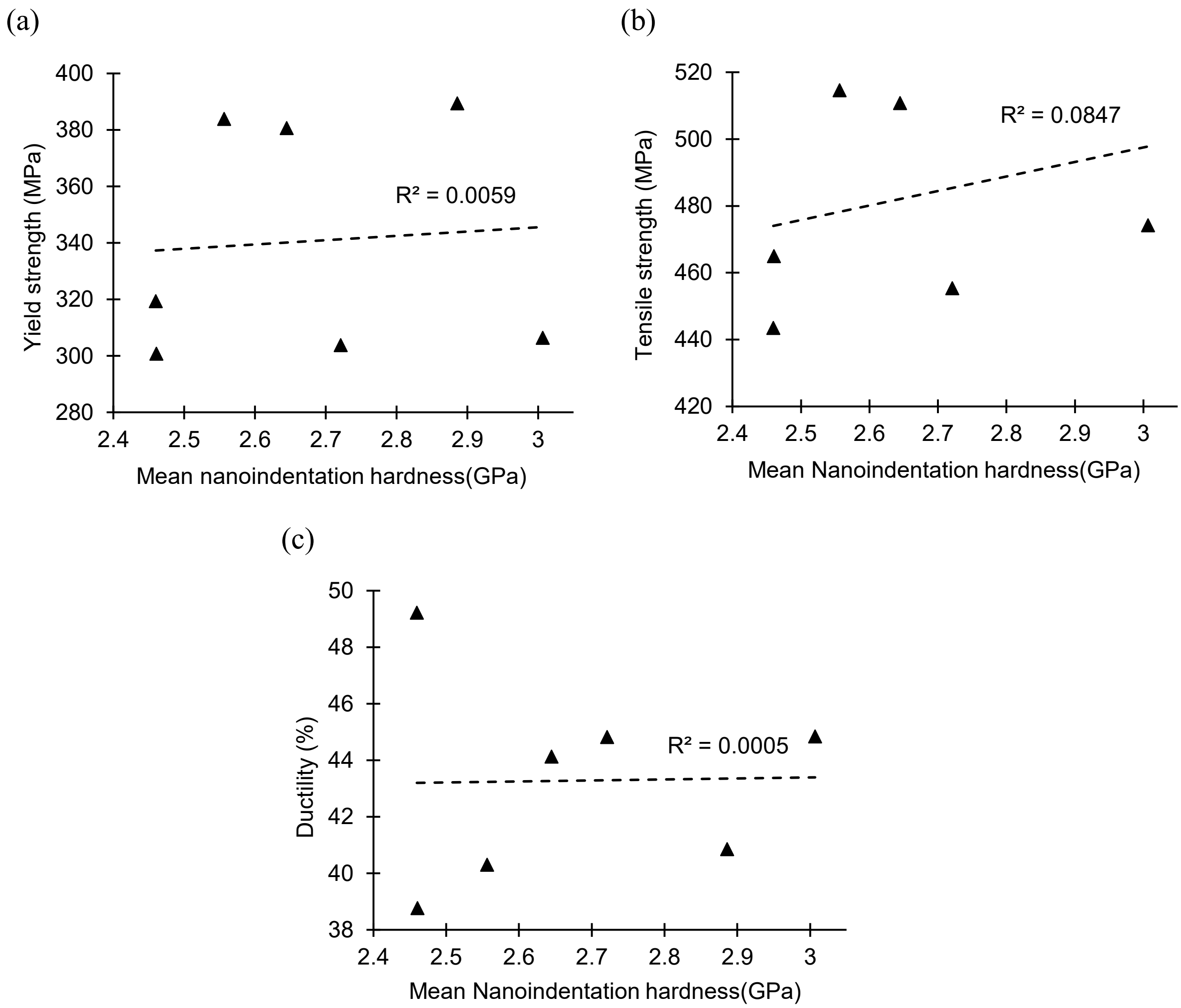

Fig. 14: Scattered plots and the linear regression fits for nanoindentation hardness (GPa) of ferrite phase and (a) yield strength (MPa), (b) tensile strength (MPa), and (c) ductility of ASTM A36 steels exposed to various elevated temperatures

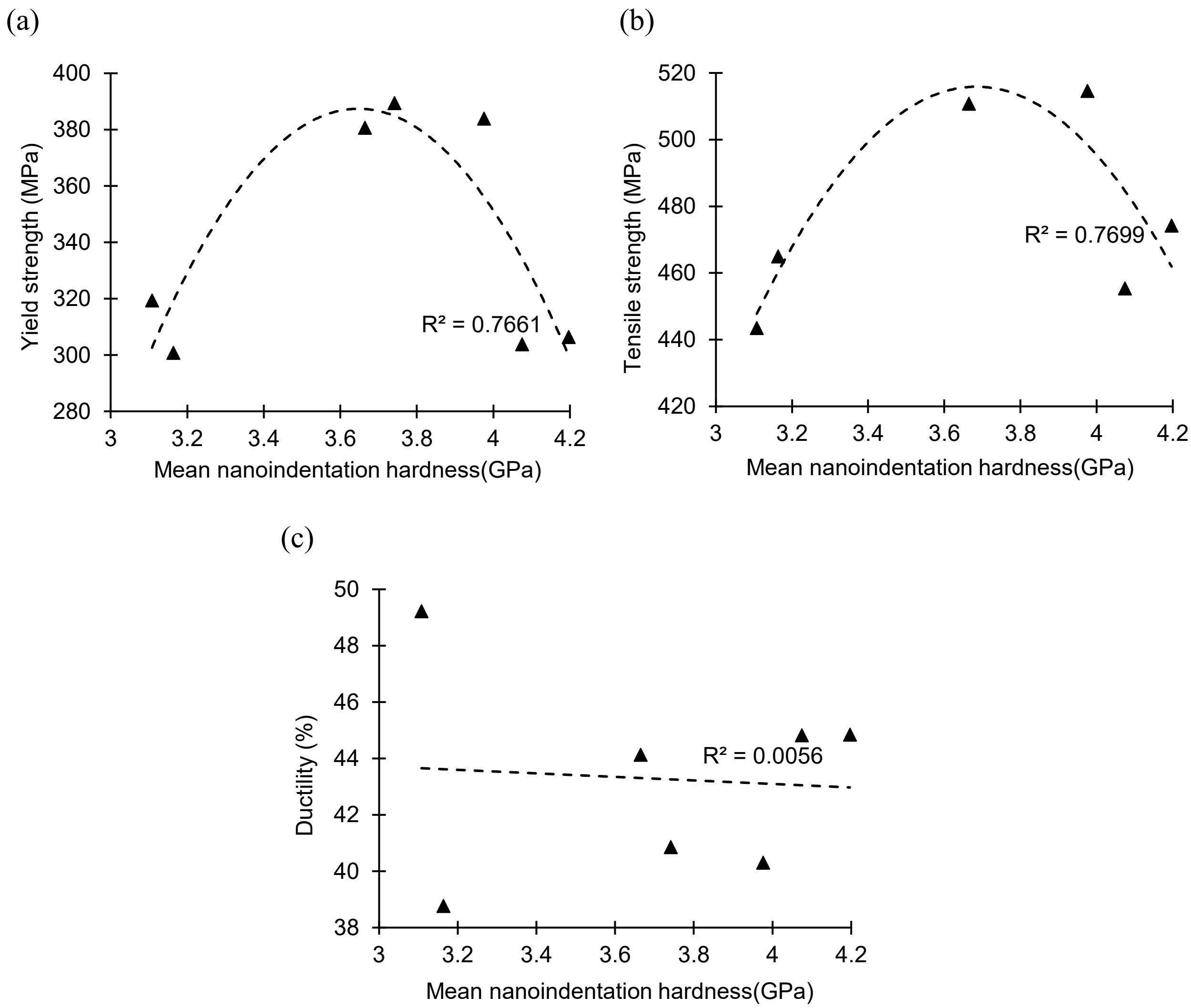

Fig. 15: Scattered plots and the regression fits for nanoindentation hardness (GPa) of ferrite phase and (a) yield strength (MPa), (b) tensile strength (MPa), and (c) ductility of ASTM A36 steels exposed to various elevated temperatures.

Table 1. A comparison of nanoindentation hardness values (GPa) of ferrite and pearlite reported in the literature

Reference	Material	Ferrite	Pearlite	Martensite	Austenite
Chen et al. 2008 (Chen et al. 2008)	TRIP steel	2.98	-	-	-
Hernandez et al. 2010 (Baltazar Hernandez et al. 2010)	Spot welded dual-phase steel	3.00	-	7.20	-
Gadelrab et al. 2012 (Gadelrab et al. 2012)	Duplex stainless steel	3.75	-	-	3.19
Pham et al. 2014 (Pham et al. 2014)	SS400 steel weld zone (bm)	2.49	4.10	-	-
Taylor et al. 2014 (Taylor et al. 2014)	DP980 steel	3.98	-	6.46	-
Pham and Kim 2015 (Pham and Kim 2015)	SM490 steel weld zone (bm)	2.72	4.06	-	-
Mazaheri et al. 2015 (Mazaheri et al. 2015)	Dual-phase steel	1.99-3.12	-	3.59-4.44	-
Schwarm et al. 2017 (Schwarm et al. 2017)	ASTM A351 stainless steel	5.00	-	-	4.80
Current Study	ASTM A36 steel	2.46-3.01	3.11-4.20	-	-

Note: bm – base metal.